



High-resolution spectral mapping of urban thermal properties with Unmanned Aerial Vehicles

Niki Gaitani ^{a,*}, Ingunn Burud ^b, Thomas Thiis ^b, Mat Santamouris ^{a,c}

^a National Kapodistrian University of Athens, Group of Buildings Environmental Studies, Building of Physics-5, University Campus, 157 84, Athens, Greece

^b Norwegian University of Life Sciences, Department of Mathematical Sciences and Technology Campus Ås, P.O Box 2003, 1433 Ås, Norway

^c The Anita Lawrence Chair, High Performing Architecture, School of Built Environment, University of New South Wales, Sydney, Australia



ARTICLE INFO

Article history:

Received 17 February 2017

Received in revised form

25 April 2017

Accepted 17 May 2017

Available online 19 May 2017

Keywords:

Urban microclimate

UAV

IR

NIR

Aerial survey

Materials

Surface temperature

ABSTRACT

The integration of microclimatic information and physical properties of the materials into urban design is essential for adequately addressing the challenges related to climate change and to adaptation of urban environment to new climatic loads. Especially, the thermal and optical properties of materials used in the urban fabric play a fundamental role in determining the microclimate and building's energy balance. The present research approach aims at analyzing the thermal characteristics of the materials and the surface temperature distribution using airborne multispectral imaging sensors mounted on Unmanned Aerial Vehicle (UAV). Aerial surveys and in-situ measurements have been carried out in April 2016 at the Municipality of Ymittos in Athens (Greece). The applied multi-sensory survey included high resolution imaging of the materials in the visible and near infrared (VIS/NIR) wavelength region and IR part of the spectrum. The images have been analysed to form maps of surface temperature distribution and of material properties. The derived thermal maps show the changes in surface temperatures of the urban materials during a diurnal heating cycle. In addition, ground measurements of VIS/NIR reflection and albedo from the survey area were obtained and an albedo map and a map of apparent thermal inertia were derived. Thermal scanning of the asphalt in the area, allowed the estimation of the state of decay due to weathering and traffic. The combined maps of surface temperature, albedo and apparent thermal inertia give new perspectives of the urban features and enhance the classification of fine urban material and the energy balance models.

© 2017 Elsevier Ltd. All rights reserved.

1. Introduction

Over half of the global population is residing in urban areas, which are at the forefront of the climate change issue [1]. Climate projections foresee additional stress in cities through increased numbers of heat waves, more intense droughts and frequent inland floods. Consistent knowledge about cities, their structure, materials and vegetation is of high relevance for urban based adaptation and mitigation strategies [2]. The Intergovernmental Panel on Climate Change [3] notes the lack of information on urban areas at detailed spatial and temporal resolution and the importance to derive comprehensive databases on cities and develop urban climate models. To understand the urban climate a thorough consideration of many parameters, such as urban morphology, land cover,

moisture availability, anthropogenic heat and material properties, is required.

Urban heat island (UHI) is the more documented phenomenon of climate change [4–6]. It refers to the occurrence of high urban temperatures compared to the surrounding rural or suburban areas. There are more than 400 cities around the world where urban heat island is experimentally documented [7], while its average magnitude may exceed 5 °C, [8]. UHI has a serious impact on the energy consumption for cooling, while it increases the concentration of pollutants and affects human health, [9].

The properties of the materials used in the urban fabric play an essential role in the energy balance, which modifies the microclimate [10]. Their thermal performance is mainly determined by the physical characteristics mainly optical and thermal [11]. The most significant factors related to radiation exchange are the albedo to solar radiation and the emissivity to long wave radiation [12]. The application of materials that present high reflectivity during summer period has gained a lot of interest during the last years as a

* Corresponding author.

E-mail address: ngaitani@gmail.com (N. Gaitani).

mitigation strategy of the heat island effect [13]. These materials commonly named as “cool materials” are characterized by high solar reflectance and infrared emittance values resulting in lower surface temperatures. New generation of reflective materials exhibit a very high capacity to decrease the surface temperature in cities and mitigate the UHI, [14]. Cool pavements refer to a range of established and emerging materials that tend to store less heat and have lower surface temperatures compared to conventional ones [15,16]. Use of cool pavements in cities in combination with other mitigation technologies may contribute to decrease the peak ambient temperature up to 2 °C, [17,18].

The surface temperature is of prime importance, as it modulates the temperature of the lowest atmospheric layers and is central to the urban energy balance. A great deal of information on surface temperatures can be obtained through thermal remote sensing imagery, e.g. Voogt and Oke [19] give a scientific overview of thermal remote sensing capabilities in urban climate. When remotely-sensed imagery is available, valuable information can be extracted on the properties of the materials. However, as the most commonly available remotely sensed measurements are from satellites and usually have a spatial resolution of several meters, they are not always suitable for modelling microclimate effects in urban areas and on individual buildings. The development of Unmanned Aerial Vehicles (UAVs) and of small spectral imaging sensors makes it possible to obtain spectrally resolved images at very high spatial resolution in an easy and flexible way.

There is an increased interest of UAVs surveying in different scientific fields as agricultural management [20,21] civil engineering [22,23] photogrammetry [24] and atmospheric environment [25]. For urban scale the use of UAVs as a sensor platform is novel and will support microscale measurements by providing flexibility in the timing of data captured and the scale of the images obtained.

The use of infrared sensors is an important tool in many close range applications. Thermal infrared cameras (in the bandwidth $3.5 \mu\text{m} < \lambda < 14 \mu\text{m}$) provide the visualization of thermal differences on the surface of an object [26]. Moreover, the integration of near infrared (NIR) camera ($0.75 \mu\text{m} < \lambda < 3 \mu\text{m}$), accumulates further radiometric information on the thermal properties of the materials [27] and is a well-established tool for the analysis of vegetation [28]. In addition, the Normal Difference Vegetation Index (NDVI) is widely adopted in vegetation studies [29] and ground parameters such as ground cover and surface water.

The aim of this study is to analyse the physical properties of materials at urban scale with high-resolution surveying and assess their mitigation potential. This paper presents a classification-based methodology for surface emissivity mapping and surface temperature distribution over the examined area by combining airborne data, in-situ measurements and emissivity values. The surface temperature maps and the solar reflectance map have been used to derive a map of apparent thermal inertia.

2. Description of the site

The study area was in Ymittos Municipality, which is a suburb, situated 2.5 km southeast from the centre of Athens, Greece. The typical Mediterranean climate in this area is characterized by hot, dry summers and cool, wet winters.

The study site was rehabilitated in the period 2012–2014. The central square (see Fig. 1), with the town-hall is located just north of a park of 34800 m^2 with an old abandoned industrial area of 157000 m^2 to the west. The initial pavements were made of old asphalt, concrete and dark paving materials, with albedo varying from 0.05 to 0.22. At final form 5170 m^2 of pavement and 4000 m^2 of asphalt were replaced. In total, over 9000 m^2 of cool paving coating and 555 m^2 of pavement with embedded photovoltaic

panels have been applied to the area. The examined area has been selected to combine: (a) an area with a small green space, the park, (b) an area with reflective pavements, the square of Ymittos and (c) a reference area with conventional material, the surrounding neighbourhoods.

Indicative points of different materials are shown in Fig. 1: asphalt with cool coating (Point 7), marble (Point 9, 10, 11), old conventional asphalt (Point 1, 3, 5, 6), new conventional asphalt (Point 4), paving tiles (Point 8) and vegetation (Point 2).

3. Materials and data

Aerial surveys and in-situ measurements have been carried out in April 2016 at the Municipality of Ymittos in Athens (Greece). The applied multisensory survey included high resolution recordings of the materials in the visible and near infrared (VIS/NIR) wavelength region and IR part of the spectrum. The flights were performed in a predetermined pattern at an altitude of 100 m. A total of approximately 80 partly overlapping images were recorded in each flight.

An RGB camera, a rebuild RGB camera where the blue channel is replaced by a NIR channel (*Canon PowerShot* rebuild by *Maxmax.com*) and an IR camera (*Optris 640*) were used. The pixel size of the pictures varied from 8 to 80 mm depending on the type of sensor.

The RGB, VIS/NIR and IR images from the aerial surveys have been corrected for the geometric distortions (orthorectification process) [30] and then transformed to geo-referenced raster images with ERDAS Imagine [31]. A standardized grey calibration plate reflecting 60% of the solar radiation was recorded before and after each set of VIS/NIR images. Close-up images of the different materials were also performed with an RGB camera, an IR camera and the VIS/NIR camera.

Additionally, in-situ measurements were conducted under sunny, calm and clear atmospheric conditions, as listed in Table 1. Not all the measurements are used in this paper.

4. Theory and analysis

The intensity of infrared radiation, which is emitted by each body, depends on the temperature as well as on the radiation features of the surface material of the measured object. For the estimation of surface temperature, the spatial distribution of urban surface emissivity is site specific, depending mainly on vegetation and man-made materials at the area.

To classify the surface material the Normalized Differential Vegetation Index (NDVI) maps were computed from the VIS/NIR images. The formulation of NDVI allows to cope with identical patches shaded (cloud sky) and non-shaded (bright sunshine), by dividing by the sum of reflectances. The NDVI algorithm subtracts the red reflectance values from the NIR and divides it by the sum of NIR and red bands according to the equation:

$$\text{NDVI} = (\text{NIR} - \text{R}) / (\text{NIR} + \text{R}) \quad (1)$$

where NIR and R are the reflectance values in the near infrared and red wavebands, respectively.

A classification map of four materials, water, asphalt, soil and vegetation (Fig. 2), was created from the NDVI map and a value of the emissivity was assigned to each class of materials [32]. The material classes have been used to calibrate IR measurements to represent actual surface temperature. In total four surface temperature maps were obtained, early morning (7:40 a.m.), late morning (10:15 a.m.), midday (13:30 p.m.) and evening (20:20 p.m.) (displayed in Fig. 3).

Albedo (or solar reflectivity) is defined as the fraction of incident radiation that is reflected by a surface and it is measured on a scale



Fig. 1. The study area in Athens, (RGB photo taken from the UAV).

Table 1

Description of in-situ measurements.

Air temperature T_{ambient} and Relative humidity RH%	(A) Data loggers (Tiny Tag TGP-4500) dual channel temperature and relative humidity, placed into weather stations (at 1.80 m height) at 3 selected sites (A, B, C) (B) Thermometer Vector Instruments type T351-PX and Hygrometer placed on telescopic mast at 3.5 m height (mobile meteorological station).
Direct solar radiation	Pyranometer Kipp & Zonen
Albedo	Albedometer Kipp & Zonen
Surface temperature	Surface thermometer (HP23-A, Hygropalm 23-Rotronic) and Thermocamera (Agema Thermovision 570. Spectral range 7.5–13 μm)
Wind speed and direction	Anemometer A100K Pulse & W200 Porton Windvane, placed on telescopic mast at 3.5 m height (mobile meteorological station)

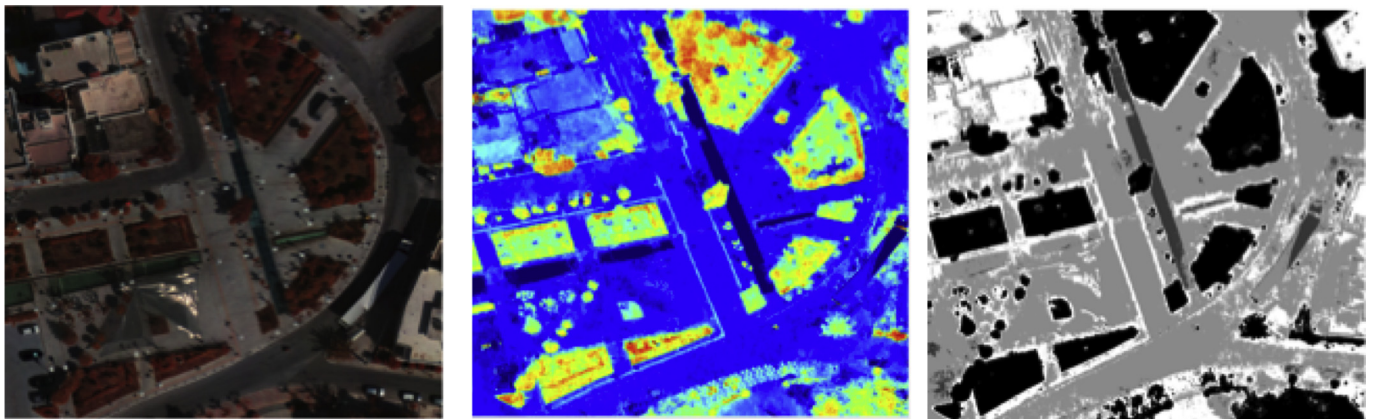


Fig. 2. (a) The area of interest recorded in the NIR band, (b) NDVI map with values from 0 (dark blue colour) to 0.8 (red colour) and (c) Emissivity classes (given in Table 2) derived from the NDVI map. (For interpretation of the references to colour in this figure legend, the reader is referred to the web version of this article.)

from 0 (no reflective) to 1 (perfect reflection). As albedo depends on the optical properties of the surface layer of the materials, it can change over time or with additives. The albedo of new paved

asphalt usually ranges between 0.04 and 0.06 [33,34] and rises with aging to 0.09–0.18 [35]. The albedo of concrete has the opposite trend, with higher value (0.35–0.40) at construction and

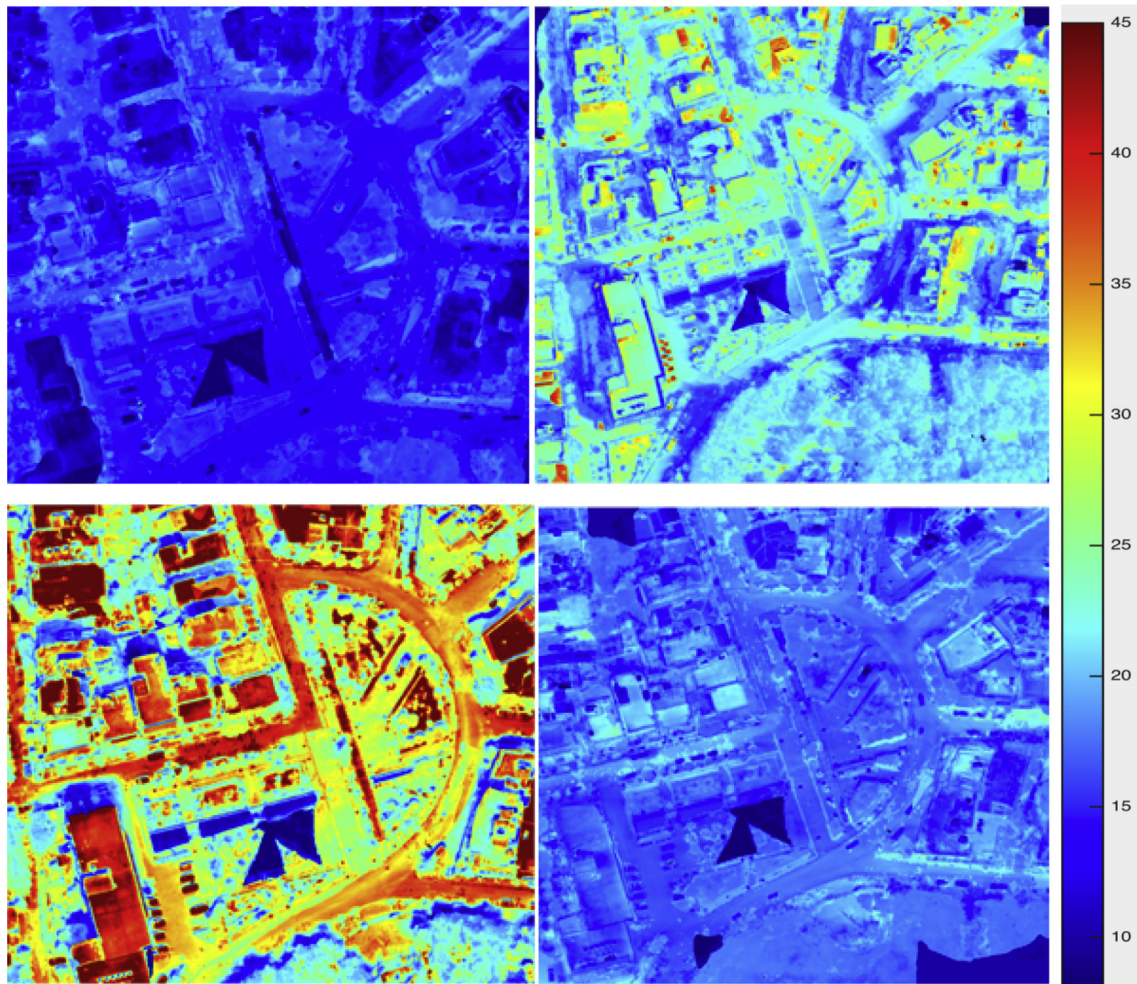


Fig. 3. Map of the surface temperature ($^{\circ}\text{C}$) distribution at (a) 7:40 a.m., (b) 10:15 a.m., (c) 13:30 p.m., (d) 20:20 p.m. Note that some areas corresponding to water, solar shading and vegetation remain at low temperatures ($<25\text{ }^{\circ}\text{C}$) throughout the day (dark blue colours). The asphalt areas and some roofs attain very high temperatures of $45\text{ }^{\circ}\text{C}$ and more in the middle of the day (red colour in image c). Marble is cooler than asphalt during the hours with solar radiation (green colour in image c). (For interpretation of the references to colour in this figure legend, the reader is referred to the web version of this article.)

decreasing over time to 0.06–0.19, because of weathering, soiling and abrasion [36]. According to studies [37] there is a reduction in the cool coatings reflectance after weathering exposure.

While reflectance is defined as this same fraction for a single incident angle, albedo is the directional integration of reflectance over all sun-view geometries. However, there have been attempts to compute albedo values directly from narrowband reflectance values from airborne imaging (G.A. Ban-Weiss et al. [38]). In this case the surface is assumed to reflect isotropically (i.e. equally at all angles). This approach was adopted to estimate albedo from our multispectral UAV measurements.

Furthermore, the surface temperature maps and the solar reflectance map have been used to derive a map of apparent thermal inertia. Thermal inertia (TI) is a measure of the responsiveness of a material to variations in temperature and it is calculated based on the knowledge of thermal conductivity and density of the near-surface layer [39].

$$\text{TI} = \sqrt{k\rho C} \quad (2)$$

where TI is the thermal inertia ($\text{J m}^{-2} \text{K}^{-1} \text{s}^{-1/2}$) of the surface material, k is the thermal conductivity ($\text{W m}^{-1} \text{K}^{-1}$), ρ is the density (Kgr m^{-3}) and C is the heat capacity ($\text{J Kgr}^{-1} \text{K}^{-1}$).

Materials with a high heat capacity display high thermal inertia consequently such materials will show small changes in temperature through the diurnal cycle [40]. In remote sensing TI is measured by diurnal changes in temperature. Apparent thermal inertia (ATI) gives a quantification of the effect of thermal inertia based on remotely sensed observations, and is in some cases used to determine the soil moisture content [41].

$$\text{ATI} = S(1 - \text{albedo})/\text{DTA} \quad (3)$$

where DTA, the diurnal temperature amplitude is derived from the maximum and minimum surface temperature observations and S is the solar correction factor defined as,

$$S = \sin\theta \sin\varphi (1 - (\tan\theta \tan\varphi)^2) + \cos\theta \cos\varphi \text{ arc} \cos(-\tan\theta \tan\varphi) \quad (4)$$

where θ is the local latitude and φ is the solar declination, which is calculated for each day of the year.

The solar correction factor [42] changes over space and time to normalize for solar flux variations with latitude and solar declination.

Table 2

Values for NDVI and emissivity.

NDVI	Emissivity class	Emissivity
−0.90 to −0.15	Water	0.99
−0.15 to 0.10	Asphalt	0.95
0.10 to 0.25	Soil	0.98
>0.25	Vegetation	0.97

5. Results and discussion

The area of interest as recorded in NIR band together with NDVI map and derived emissivity classes are shown in Fig. 2.

The NDVI values and the corresponding emissivity for the four classes are listed in Table 2. For the analysis, the selected examined points are non-shaded during the whole day.

The absolute surface temperatures for all the pixels in the IR maps were then computed using the correct emissivity, yielding four maps from the flights at different hours during the same day (12.04.16, 07:30 at sunrise, 10:30, 14:30 and 20:00 just after sunset). The spatial distributions of surface temperatures are shown in Fig. 3.

The first recording of temperatures (taken at sunrise), shows that the various surfaces cool off differently during the night. Generally at dawn, surface temperatures in the vegetated areas are higher than the paved surfaces which again are higher than most of the building roofs. The map changes during the course of the day, and at noon, the temperatures of the roofs are generally higher than the ones of paved surfaces, which again are higher compared to the ones of the vegetated areas.

The maps obtained at various times of the day had shades at different locations. With many recordings during the day the effect of the shades has been minimized by combining the non-shaded

parts of the stack of maps. This is an advantage of the methodology of using UAVs where multiple recordings easily can be carried out.

In order to look at the temperature variations during the day, one may take the difference between pairs of temperature maps. A more general approach however, is to perform a Principal Component Analysis (PCA) of the stack of temperature maps. PCA is a common method within multivariate statistics for reducing the dimensionality of large data sets [43]. PCA often is used to bring out strong patterns in datasets. In the present study, with the stack of temperature maps, the first PC score image yields a map of the temperature variations for the different areas.

The first principal component of a stack of images will output an image indicating the pixels with the largest variance with highly positive or negative values. The pixels with little or no variations will have a score value close to zero. The PCA was performed on the stack of four temperature images by first defolding the images to vectors, then computing the PCA regarding each pixel as a sample and the four time periods as variables. Then the unfolded score matrices are refolded to 2-dimensional images.

The PCA score image of the stack of the four calibrated surface temperature maps shown in Fig. 4 reveals the dominant patterns of the surface temperature variations during the day across the area.

The high scores represent large variation (streets and buildings), while low scores indicate low variation. The marble, which is the main material of the examined square at the Ymittos (indicated in the Fig. 1) presents low score values and has a comparative small temperature difference during the day accordingly.

Fig. 5 gives the diurnal variation of mean surface temperature distributions of vegetation, asphalt and marble. During the survey the air temperature was between 14.0 °C and 28.2 °C and the relative humidity from 31% to 80%. The lowest temperature was measured at the green areas with average value close to air

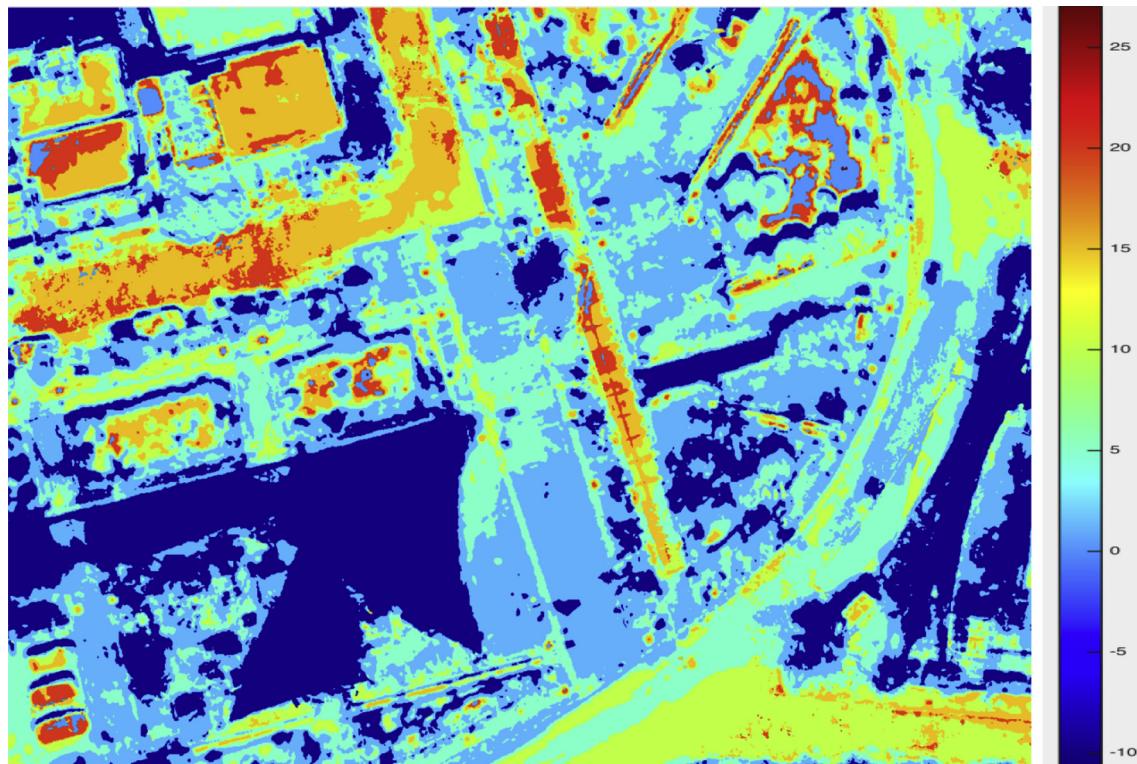


Fig. 4. Close-up of score image from first principal component of the PCA. Observe that areas with high surface temperature difference are in red colour and low surface temperature difference are in dark blue. (For interpretation of the references to colour in this figure legend, the reader is referred to the web version of this article.)

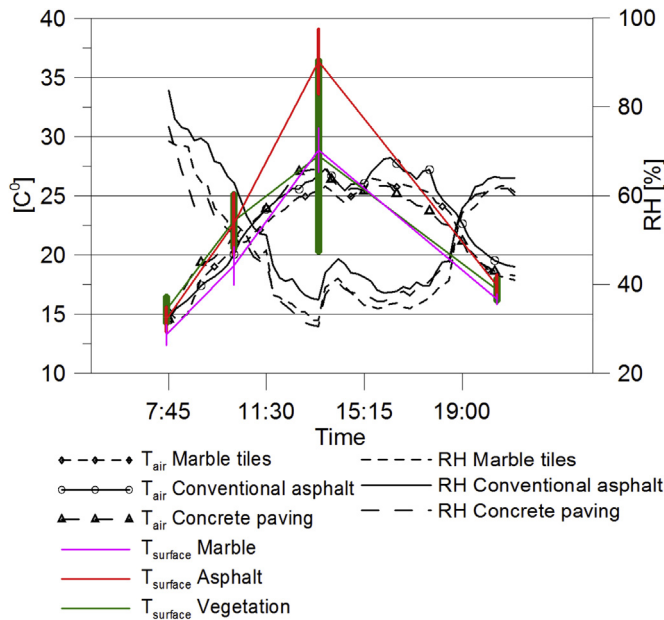


Fig. 5. The diurnal variation of surface temperature of vegetation, asphalt, and marble from aerial survey and the diurnal variation of air temperature and relative humidity from weather stations. Coloured lines indicate mean surface temperature of 50 points, error bars show standard deviation. In addition the diurnal variation of air temperature and relative humidity as measured at three locations of the study area is given in black-white. The weather stations were placed at three points of interest with different surface features on 12.04.16. (For interpretation of the references to colour in this figure legend, the reader is referred to the web version of this article.)

temperature. In addition, the marble presents relatively low surface temperature with mean temperature at noon close to 28°C as a result of its colour, texture and the higher solar reflectance.

The large standard deviation at noon is due to the great variety of vegetation at the examined area and different heights of the trees. Tree tops might cast small shadows on the ground vegetation that our resolution will not capture; however, the pixel values will be affected by these small shadows. The vegetation on the ground was not homogenous.

The albedo at the site was measured in the middle of the day with a dual-pyranometer for a set of different materials and the averaged values are given at Table 3 together with the corresponding values of NDVI and ATI. Moreover, the remotely sensed reflectance values were used to compute the mean albedo map of the area (Fig. 6). The model used for deriving the albedo from the UAV pictures was calibrated with data from a specific camera [38]. The accuracy in this model is from 0.00 to 0.01 at low albedo to 0.06–0.14 at high albedo. Using a different camera with a different range of the spectral bands will introduce an error which is not estimated here due to lack of extensive ground data.

The relatively high measured albedo values of the asphalts at the

site indicate the large exposure to weathering. Weatherisation of the reflecting materials is due to the accumulation of dust, soot particles and biomass, exposure to ultraviolet radiation, microbial growth, moisture penetration and condensation, [44]. The old asphalt's albedo was measured to 0.17 while the more recent (two years old) asphalts, both the conventional and the one with cool coating, have values of 0.12. These values point out the weathering effects and degradation of the streets due to the high traffic at the area. As noted in the literature survey previously [36], conventional asphalt initially has a low albedo (~ 0.05), increasing with ageing and exposure. Contrary to the asphalt, the cool coating has a high initial albedo which decreases due to surface staining and material degradation. To further explore the thermal gradient of the materials, the surface temperatures (Fig. 3) and the solar reflectance maps (Fig. 6) have been used to derive a map of apparent thermal inertia (as shown in Fig. 8). In general, materials with high apparent thermal inertia show small changes in temperature through the diurnal cycle.

Fig. 7 shows the calculated values of apparent thermal inertia (ATI), which is a quantification of the effect of thermal inertia on soil surface temperature. ATI makes use of the surface temperature difference as well as surface albedo information.

To illustrate the thermal characteristics of the urban surfaces (albedo, thermal inertia) and the variation of their surface temperatures, close-up images are given in Fig. 8. Fig. 8a and b (surface temperature) were derived as close ups from Figs. 3 and 8c (albedo) and 8d (apparent thermal inertia) were derived as close ups from Figs. 6 and 7 respectively.

In Fig. 8b, focusing on the part of the street exposed to higher traffic marked with a circle, it is evident that the surface temperature at noon is considerably higher than the unexposed asphalt and that this is mainly due to the respectively lower albedo values resulting from accumulation of traffic residue on the asphalt. Fig. 8a shows that the surface temperature early in the morning is still affected by the previous day's energy balance. The tactile tiles (point 3) have a higher temperature than the marble (point 4), as well as the darker parts of the asphalt (point 1). Observe that the tactile tiles and the marble have albedo in the same range, but there is a difference in ATI, as marble has the higher thermal conductivity compared to the other examined materials (asphalt, concrete, and vegetation), giving rise to this difference in surface temperature between the two materials. Fig. 8d shows that the ATI of the asphalt does not vary significantly, and that the difference in surface temperature of the asphalt in the marked corner of Fig. 8b is exclusively a result of the differences in albedo. On the contrary, the difference in surface temperatures of the tactile paving tile and the marble are mainly caused by difference in ATI.

Fig. 9 shows the relation between the calculated values albedo from UAV and the diurnal surface temperature amplitude $DTA_{surface}$. The data points are grouped into clusters. By selecting the different intervals of albedo and DTA values and displaying their spatial location on the RGB orthophoto we were able to identify the

Table 3
Values from close-up images at the study area.

Material	NDVI [-]	In-Situ measured albedo	UAV calculated albedo	ATI
'New' conventional asphalt	0.05	0.12	0.20	0.53
Old conventional asphalt with 'cool' coating	-0.13	0.12	0.17	0.55
Old conventional asphalt	-0.03	0.17	0.24	0.54
Concrete	0.02	—	0.30	0.55
Marble	0.014	0.38	0.37	0.66
Tactile paving tile for blind	0.23	0.30	0.33	0.57
Vegetation	0.56	0.21	0.18	0.09



Fig. 6. The spatial distribution of calculated albedo.

type of material corresponding to each cluster of points. The figure indicates that as the albedo decreases, more of the solar radiation will be absorbed, which will increase the diurnal surface temperature amplitude $DTA_{surface}$ of the materials, except for the vegetation. When albedo increases above 0.55, the mean $DTA_{surface}$ is close to the diurnal temperature amplitude of the ambient air DTA_{air} (Fig. 5). This indicates that for materials with albedo >0.55 the radiative heat transfer is less important than convective heat transfer in the urban environment. However, the data also shows that at the site of measurements, the majority of the surfaces has albedo <0.40 , something which might weaken this observation.

The ratio of surface temperature to ambient temperature $T_{surface}/T_a$ of a position gives an indication of the sensitivity of a material to change temperature as it is exposed to solar radiation. The thermal inertia and the ATI are also important factors in explaining this phenomenon.

Fig. 10 shows the relation between $T_{surface}/T_a$ and ATI at noon. The air temperature T_a is taken as 26° which is the mean value of the three meteorological stations in the area. The figure shows that as ATI increases above 0.12, the ratio $T_{surface}/T_a$ approaches 1, thus indicating that the effect of solar radiation on surface temperature is of low importance on urban materials with ATI >0.12 . The figure also shows points of $T_{surface}/T_a < 1$, which is typical for vegetation, where solar radiation induces evapotranspiration.

Fig. 10 also shows the ratio of $T_{surface}/T_a$ and ATI at the three specific points at which the weather stations are placed. The air temperature is here taken as the reading of the weather station. The values at the weather stations follow the distribution of the UAV mapped points.

Fig. 11 shows the mean values of albedo, ATI and $DTA_{surface}$. Knowing that the diurnal air temperature amplitude DTA_{air} is approximately 14° , the data suggests that data points in the area marked A are marginally affected by the solar load, Points in area B are partly affected by solar loads and points in area C are largely affected by the solar loads.



Fig. 7. The spatial distribution of apparent thermal inertia.

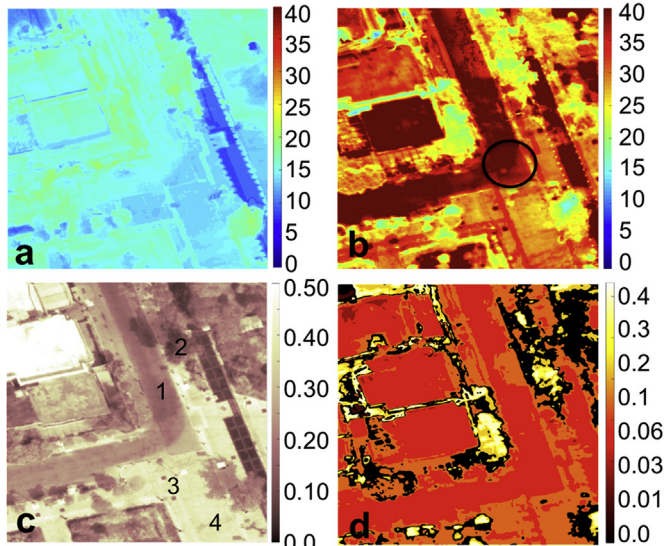


Fig. 8. Close-ups of surface temperature (8a in the morning, 8b at noon), albedo (8c) and apparent thermal inertia (8d). Indicative points of the examined materials 1. Asphalt, 2. Paving tiles, 3. Tactile tiles, 4. Marble.

6. Concluding remarks

The integration of sensors on UAVs provided an enhanced and flexible measured survey solution with accurate data captured on site. Results demonstrate that the high resolution imagery obtained gives more detailed thermal information which is essential to

classify urban material and assess surface energy balance. Some observations drawn by the fine-scale urban maps could be summarized:

- Thermal scanning of Ymittos' urban area, allowed the collection of information as to the elements, characteristics of materials, and state of decay due to weathering or man-made alterations;
- NDVI can be used to classify materials with different emissivity values;
- The PCA score image of the stack of the calibrated surface temperature reveals the dominant patterns of the surface temperature variations during the day across the area;
- As to the surface temperature distribution of different materials, the lowest temperature was measured at the green areas with average value close to air temperature. The marble was the coolest material at the square with mean value at noon close to 28 °C;
- The combined maps of solar reflectance, surface temperature and thermal inertia ease the understanding of relations between different physical properties and features of the materials;
- The changes in surface temperatures during a diurnal heating cycle varies with the materials involved and depends on the albedo and apparent thermal inertia. Especially for the materials with albedo greater than 0.55 and ATI higher than 0.12, it was demonstrated that radiative heat transfer is less important than convective heat transfer.

The findings are applicable and fundamental in the process of bioclimatic urban planning. By covering a wider spectral range with high spatial resolution up to centimetres, the new measurement capabilities with the integrated methodology will advance the:

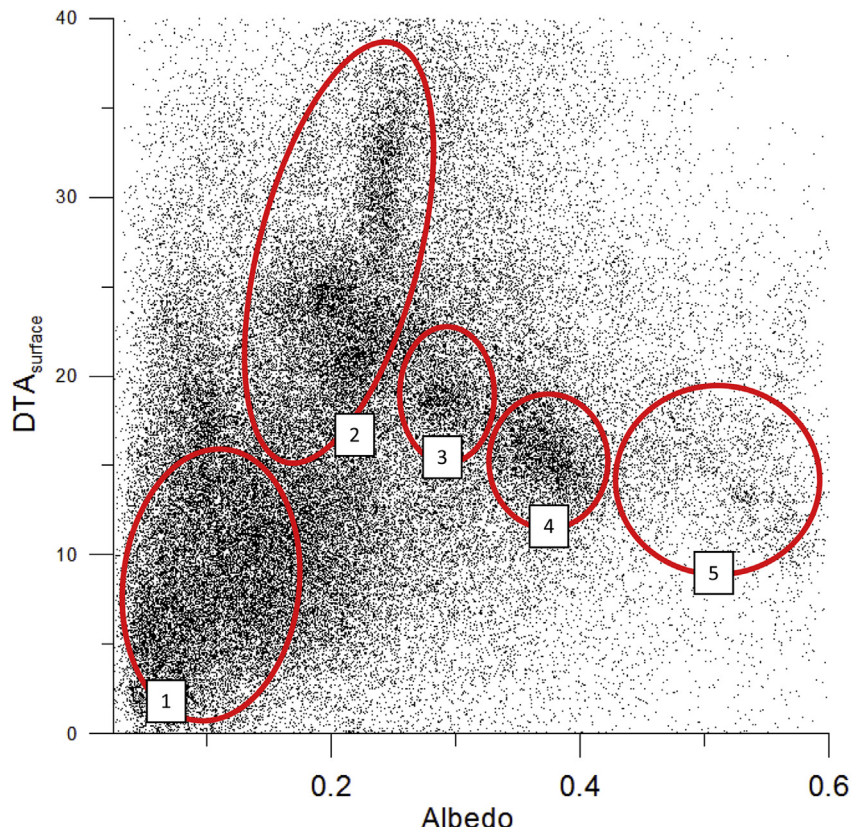


Fig. 9. Observed relation between Diurnal Surface Temperature Amplitude ($DTA_{surface}$) and Albedo. Typical values corresponding to materials 1) Vegetation 2) Asphalt and asphalt roofing 3) Concrete tiles 4) Marble 5) Reflective roof.

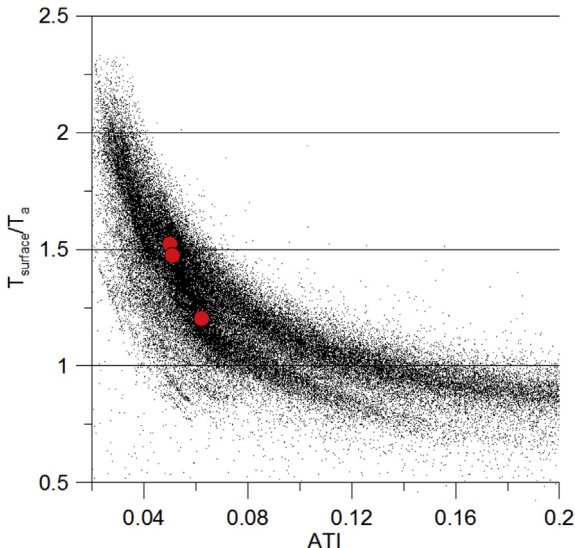


Fig. 10. The ratio of surface temperature to air temperature (T_{surface}/T_a) and the apparent thermal inertia (ATI). Each black point represents the measured values from the aerial images divided by the mean air temperature and the red points represent the in-situ measured values of surface and air temperature.

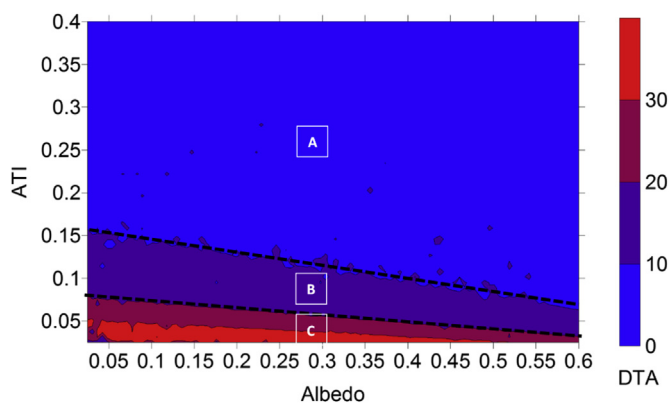


Fig. 11. Apparent thermal inertia ATI and broadband albedo a_o (DTA_{surface}) is derived from the two daily land surface temperature observations. Materials with a high heat capacity display high thermal inertia consequently such materials will show small changes in temperature through the diurnal cycle.

- Development of classified maps with physical properties of the materials at neighbourhood scale revealing the complex mechanisms that lead to microclimatic modifications and to quantify their relative contribution;
- 3D modelling, validation and computation of surface parameters for urban planning;
- Evaluation of the implementation phases of rehabilitation projects;
- Exploration of the man-made alterations;
- Study of the weathering effect on the degradation of the surfaces;
- Decision making of micro-climatic design

The multisensory technique applied in the present work demonstrates how the novel advances in sensor development combined with advanced data analysis provide a new and unique tool for urban climate studies. Overall the proposed method was proved to be low-cost and feasible for studying the micro urban thermal environment.

References

- [1] United Nations, World Urbanization Prospects: the 2014 Revision, United Nations, NY, 2014.
- [2] B. Bechtel, et al., ISPRS Int. J. Geo Inf. 4 (2015) 199–219.
- [3] IPCC, 2014. http://www.ipcc.ch/pdf/assessment-report/ar5/wg2/WGIIAR5-FrontMatterA_FINAL.pdf.
- [4] A.H. Rosenfeld, H. Akbari, S. Bretz, B.L. Fishman, D.M. Kurn, D. Sailor, H. Taha, Mitigation of urban heat islands: materials, utility programs, updates, Energy Build. 22 (1995) 255–265.
- [5] M. Kolokotroni, I. Giannitsaris, R. Watkins, The effect of the London urban heat island on building summer cooling demand and night ventilation strategies, Sol. Energy 80 (2006) 383–392.
- [6] N.H. Wong, S.K. Jusuf, N.I. Syafii, Y. Chen, N. Hajadi, H. Sathyaranayanan, Y.V. Manickavasagam, Evaluation of the impact of the surrounding urban morphology on building energy consumption, Sol. Energy 85 (2011) 57–71.
- [7] M. Santamouris, Innovating to zero the building sector in Europe: minimising the energy consumption, eradication of the energy poverty and mitigating the local climate change, Sol. Energy 128 (2016) 61–94.
- [8] M. Santamouris, Analyzing the heat island magnitude and characteristics in one hundred Asian and Australian cities and regions, Sci. Total. Environ. 512–513 (2015) 582–598.
- [9] M. Santamouris, Regulating the damaged thermostat of the cities – status, impacts and mitigation challenges, Energy Build. 91 (2015) 43–56.
- [10] A. Kakoniti, et al., The role of materials selection in the urban heat island effect in dry mid-latitude climates, Environ. Fluid Mech. 16 (2016) 347–371.
- [11] L. Doulous, M. Santamouris, I. Livada, Passive cooling of outdoor urban spaces. The role of materials, Sol. Energy 77 (2004) 231–249.
- [12] A. Rasheed, et al., Int. J. Climatol. 31 (2) (2011) 289–301.
- [13] M. Santamouris, Using cool pavements as a mitigation strategy to fight urban heat island – a review of actual developments, Renew. Sustain. Energy Rev. 26 (2013) 224–240.
- [14] M. Santamouris, et al., Using advanced cool materials in the urban built environment to mitigate heat islands and improve thermal comfort conditions, Sol. Energy 85 (2011) 3085–3102.
- [15] D. Kolokotsa, M. Santamouris, H. Akbari, Advances in the development of cool materials for the built environment. Cool Pavements, pp. 104–119, DOI: <http://dx.doi.org/10.2174/9781608054718113010008>, ISBN: 978-1-60805-597-5.
- [16] S. Bretz, H. Akbari, Long-term performance of high albedo roof coatings, Energy Build. 25 (1997) 156–167.
- [17] M. Santamouris, et al., Passive and active cooling for the outdoor built environment – analysis and assessment of the cooling potential of mitigation technologies using performance data from 220 large scale projects, Sol. Energy (in press), <http://dx.doi.org/10.1016/j.solener.2016.12.006>
- [18] M. Santamouris, N. Gaitani, A. Spanou, M. Saliari, K. Gianopoulou, K. Vasilakopoulou, Using cool paving materials to improve microclimate of urban areas – design realisation and results of the flisvos project, Build. Environ. 53 (2012) 128–136.
- [19] J.A. Voogt, T.R. Oke, Remote Sens. Environ. 86 (37) (2003) 370–384.
- [20] J. Cago, et al., UAVs challenge to assess water stress for sustainable agriculture, Agric. Water Manag. 153 (2015) 9–19.
- [21] P.J. Zarco-Tejada, et al., Tree height quantification using very high resolution imagery acquired from an unmanned aerial vehicle (UAV) and automatic 3D photo reconstruction methods, Eur. J. Agron. 55 (2014) 89–99.
- [22] S. Siebert, T. Jochen, Mobile 3D mapping for surveying earthwork projects using an Unmanned Aerial Vehicle (UAV) system, Autom. Constr. 41 (2014) 1–14.
- [23] A. Nishar, et al., Thermal infrared imaging of geothermal environments and by an unmanned aerial vehicle (UAV): a case study of the Wairakei – Tauhara geothermal field, Taupo, New Zealand, Renew. Energy 86 (2016) 1256–1264.
- [24] I. Colomina, P. Molina, Unmanned aerial systems for photogrammetry and remote sensing: a review, ISPRS J. Photogramm. Remote Sens. 92 (2014) 79–97.
- [25] Z.R. Peng, A study of vertical distribution patterns of PM 2.5 concentrations based on ambient monitoring with unmanned aerial vehicles: a case in Hangzhou, China, Atmos. Environ. 123 (2015) 357–369.
- [26] M. Ivan Alba, et al., Mapping infrared data on terrestrial laser scanning 3D models of buildings, Remote Sens. 3 (2011) 1847–1870.
- [27] P. Berdahl, S.E. Bretz, Preliminary survey of the solar reflectance of cool roofing materials, Energy Build. 25 (1997) 149–158.
- [28] E.S. Cozza, M. Alloisio, A. Comite, G. Di Tanna, S. Vicini, NIR-reflecting properties of new paints for energy-efficient buildings, Sol. Energy 116 (2015) 108–116.
- [29] A. Holme, D.G. Burnside, D.G. A.A. Mitchell, The development of a system for monitoring trend in range condition in the arid shrub lands of Western Australia, Aust. Rangel. J. 9 (1987) 14–20.
- [30] M. Jaud, et al., Method for orthorectification of terrestrial radar maps, ISPRS J. Photogramm. Remote Sens. 97 (2014) 185–194.
- [31] <http://www.hexagongeospatial.com/products/producer-suite/erdas-imagine>.
- [32] R. Oltra-Carrio, J.A. Sobrino, B. Franch, F. Nerry, Land surface emissivity retrieval from airborne sensor over urban areas, Remote Sens. Environ. 123 (2012) 298–305.
- [33] H. Taha, et al., High Albedo Materials for Reducing Building Cooling Energy

- Use, Lawrence Berkley Lab, Berkley, CA, 1992.
- [34] Li, et al., Field measurement of albedo for different land cover materials and effects on thermal performance, *Build. Environ.* 59 (2013a) 536–546.
 - [35] S. Sen, J. Roesler, Aging albedo model for asphalt pavement surfaces, *J. Clean. Prod.* 117 (2016) 169–175.
 - [36] R. Levinson, et al., Effects of composition and exposure on the solar reflectance of Portland cement concrete, *Cm. Concr. Res.* 32 (2002) 1679–1698.
 - [37] K. Dornelles, R. Caram, E. Sichieri, Natural weathering of cool coatings and its effect on solar reflectance of roof surfaces, 6th Int. Build. Phys. Conf. IPBC, Energy Procedia 78 (2015) 1587–1592.
 - [38] G.A. Ban-Weiss, et al., Using remote sensing to quantify albedo of roofs in seven California cities, Part1: Methods, *Sol. Energy* 115 (2015) 777–790.
 - [39] T.-Y. Chang, et al., Estimation of root zone soil moisture using apparent thermal inertia with MODIS imagery over a tropical catchment in Northern Thailand, *IEEE J. Sel. Top. Appl. Earth Obs. Remote Sens.* 5 (2012) 752–761, <http://dx.doi.org/10.1109/JSTARS.2012.2190588>.
 - [40] M. Sohrabinia, et al., Soil moisture derived using two apparent thermal inertia functions over Canterbury, New Zealand, *J. Appl. Remote Sens.* 8 (1) (May 22, 2014), <http://dx.doi.org/10.1117/1.JRS.8.083624>, 083624.
 - [41] Y. Qin, Pavement surface maximum temperature increases linearly with solar absorption and reciprocal thermal inertia, *Int. J. Heat Mass Transf.* 97 (2016) 391–399.
 - [42] J. Van doninck, et al., *Int. J. Appl. Earth Obs. Geoinf.* 13 (2011) 934–941.
 - [43] S. Wold, K. Espensen, P. Geladi, Principal component analysis, *Chemom. Intell. Labo. Syst.* 2 (1987) 37–52.
 - [44] E. Mastrapostoli, et al., On the aging of cool roofs. Measure of the optical degradation, chemical and biological analysis and assessment of the energy impact, *Energy Build.* 114 (15) (2016) 191–199.